Chemical Geology 670 (2024) 122438

Contents lists available at ScienceDirect

Chemical Geology

journal homepage: www.elsevier.com/locate/chemgeo

2D geochemical imaging of biogenic marine carbonates using LA-TOF-ICP-MS at 1 and 2 μm pixel resolution

Christopher D. Standish [a,*], J. Andy Milton [a], Tessa M. Page [a], Rachel M. Brown [a], David Douglas [b], Bence Paul [b,c], Lukas Schlatt [d], Gavin L. Foster [a]

[a] School of Ocean & Earth Sciences, University of Southampton, National Oceanography Centre, European Way, Southampton SO14 3ZH, UK
[b] Elemental Scientific Lasers LLC, Old Buffalo Trail, Bozeman, MT 59715, USA
[c] School of Geography, Earth and Atmospheric Sciences, The University of Melbourne, Parkville, Victoria, Australia.
[d] Nu Instruments, Clywedog Road South, Wrexham LL13 9XS, UK.

ARTICLE INFO

Editor: Oleg Pokrovsky

Keywords:
Marine carbonates
Imaging
E/Ca
Time-of-flight
Laser ablation

ABSTRACT

Many applications at the forefront of the study of the chemical composition of marine carbonates require in-situ micro-scale geochemical imaging. Such analyses are, however, challenging, requiring analytical techniques that are either expensive with limited accessibility (e.g. synchrotron X-Ray spectroscopy and secondary ion mass spectrometry), or time-consuming and able to only analyse a limited range of elements (e.g. electron microprobe). Laser ablation inductively coupled plasma mass spectrometry (LA-ICP-MS) as a tool for generating 2D images has grown in popularity, yet many analytical issues remain when generating high-spatial resolution geochemical images using this approach. Here we employ the imageGEO193 (ESL) fast wash-out laser ablation system coupled to the Nu Instruments Vitesse Time-of-Flight (TOF) ICP mass spectrometer, with its near-full mass spectra capabilities, to generate 2D geochemical images of a range of biogenic carbonates at ≤2 μm pixel resolution (pixel widths of either 1 or 2 μm) and at an unprecedented speed (200 pixels/s). We demonstrate sensitivity of ~100 cps/μg g^{-1} at low mass rising to ~1000 cps/μg g^{-1} at high mass based on analyses of reference materials JCp-1 (carbonate) and NIST SRM612 (silicate) with 1 μm wide square laser beams, and accuracy of ±7 % for elements present at concentrations >0.5 μg g^{-1} based on analyses of carbonate reference material JCt-1. By applying our quantitative method to a range of biogenic carbonates (coral skeletons, coralline algae, foraminifera), we demonstrate that considerable but coherent micron-scale compositional variability is the norm for nearly all quantified elements, including: Mg, Sr, Ba and U. This approach therefore has great potential to provide valuable insights into biomineralisation mechanisms and "vital effects", ultimately facilitating more robust reconstructions of past environments.

1. Introduction

A wide variety of marine organisms such as fish, corals, clams, and foraminifera make shells or hard parts from calcium carbonate ($CaCO_3$), in the form of calcite or aragonite. The chemical composition of these biogenic carbonates reflects both the calcification mechanisms responsible for the formation of the biomineral (Erez, 2003) and the prevailing environment in which the biomineral formed (Thompson, 2022). As a result, the chemical composition of ancient biominerals are an important archive of past climate change (Elderfield et al., 2012). However, exactly how the calcification process influences biomineral chemical composition is rather poorly understood and deviations from inorganic equilibria have long been grouped under the umbrella term "vital effects" (Urey et al., 1951). A common observation across taxa is that vital effects become more dominant as you move from the population scale to the individual scale, and from bulk whole sample measurements to micron-scale in situ determinations of composition (Eggins et al., 2004; Fehrenbacher et al., 2020; Sadekov et al., 2009). While this presents a fundamental challenge to high resolution climate reconstructions based on in situ sampling of incrementally grown substrates (e.g. corals and coralline algae), it allows fine-scale measurements of composition to provide valuable and novel insights into the nature of vital effects and hence the physiological processes that ultimately drive them (Bonnin et al., 2019; Chalk et al., 2021; Meibom et al., 2004). For the latter

* Corresponding author.
E-mail address: c.d.standish@soton.ac.uk (C.D. Standish).

https://doi.org/10.1016/j.chemgeo.2024.122438
Received 30 April 2024; Received in revised form 30 September 2024; Accepted 1 October 2024
Available online 3 October 2024

application in particular, 2D maps, rather than discrete measurements, are particularly useful as they not only allow a visualisation of the small-scale elemental variations present but also enable robust links to be made across imaging modalities providing novel mechanistic insights into biomineralisation (Chalk et al., 2021; Chen et al., 2023; Fietzke et al., 2015; Fietzke and Wall, 2022; Flöter et al., 2022; Meibom et al., 2004; Standish et al., 2024).

There are a number of methods currently available for the 2D mapping of the chemical composition of marine carbonate biominerals at the micron-scale, and these include electron microprobe analysis (EMPA: Fehrenbacher and Martin, 2014; John et al., 2023), synchrotron X-Ray spectroscopy (Limburg et al., 2007, 2011; Branson, 2018), and secondary ion mass spectrometry (SIMS: Chen et al., 2023; Meibom et al., 2004). While synchrotron techniques are capable of generating 2D (and 3D) maps of elemental composition at <1 μm pixel resolution, access to these large facilities is often restricted and only a limited range of elements can typically be analysed on any given beam line (e.g. Branson et al., 2013, just imaged Mg). Consequently, only nano-scale SIMS (nanoSIMS and TOF-SIMS) and EMPA are routinely used for generating 2D maps of marine biominerals such as corals and foraminifera at sub-5 μm pixel (Bonnin et al., 2019; Chen et al., 2023; Meibom et al., 2004, 2008). These techniques also have their limitations, for instance EMPA is only able to detect major elements (e.g. Mg, Ca and Sr), collecting maps can be time consuming (e.g. 2 pixels/s: Eggins et al., 2004), and accuracy has recently been questioned (Balestra et al., 2021). While nanoSIMS and TOF-SIMS can detect a wider range of elements and isotopes (Chen et al., 2023), and mapping is generally quicker (100 pixels/s: Chen et al., 2023), multiple imaging frames are typically collected to accumulate enough counts to detect elements present at trace quantities. For example, Chen et al. (2023), using nanoSIMS, collected a minimum of 4 frames for each image resulting in integrated speeds of <25 pixels/s. In both instances, this slow speed of image acquisition restricts the size of the areas typically mapped (<2000 μm^2), limiting the quality of the insights that can be gathered.

Laser ablation inductively coupled plasma mass spectrometry (LA-ICP-MS) is widely acknowledged as a powerful micro-analysis technique across the geo-, environmental, forensic, and medical sciences (Almirall and Trejos, 2016; Barbosa and Sussulini, 2019; Müller and Fietzke, 2016; Standish et al., 2013; Sylvester and Jackson, 2016). While 2D maps can be generated using this technique (Chalk et al., 2021; Fietzke et al., 2015), they are frequently not at sub-10 μm scale and are slow to generate (~5 pixels/s). These limitations both arise because of the relatively slow duty cycle of a quadrupole ICP-MS, where it gradually scans from low mass to high mass, resulting in proportionally more time spent cycling the quadrupole relative to counting ions as the pixel acquisition speed increases. 2D imaging using LA-ICP-MS is also plagued by well-known imaging artefacts (van Elteren et al., 2018) that are also partly caused by the quadrupole duty cycle but also because 2D maps are generated by continuously moving the sample below a continuously pulsing laser beam to generate a steady ion beam. Mixing of neighbouring pixels occurs because of the necessary overlapping of laser spots resulting from continuous acquisition and because the ablated material from each laser pulse can take up to several seconds to exit the ablation chamber and enter the plasma ion source (Aonishi et al., 2018). Together these tend to distort the 2D images generated. Three recent developments overcome these limitations: (i) improvements in laser cell design and ablation plume delivery now rapidly deliver ablated material to the ICP allowing millisecond washouts for single ablation pulses and increasing signal to noise (Gundlach-Graham and Günther, 2016; Van Malderen et al., 2016); (ii) Time-of-Flight (TOF) ICP mass spectrometers allow the collection of near full mass spectrum many thousands of times per second fully resolving the short transient signals generated by the new generation of ablation cells (Van Malderen et al., 2020); and (iii) laser ablation systems have been developed that are able to fire laser pulses at >250 Hz for extended periods (Van Malderen et al., 2020). Together, these developments have facilitated the rapid generation — up to 1000 pixels/s — of high-resolution 2D elemental maps of a variety of materials including geological and biological (Van Malderen et al., 2020). Here we exploit these recent advances to generate accurate (±7 %) 2D elemental maps of a range of marine biominerals at an unprecedented spatial resolution (1–2 μm pixels) and acquisition speed (200 pixels/s).

2. Materials and methods

2.1. Samples and reference materials

Instrumental set-up and standardisation employed silicate reference materials NIST SRM610 and NIST SRM612 and a pressed nanopellet of JCp-1, a powdered *Porites* sp. coral from the Geological Survey of Japan (Okai et al., 2002). 2D geochemical imaging by LA-TOF-ICP-MS is demonstrated on a variety of marine carbonates: 1) a pressed nanopellet of JCt-1, a powdered *Tridacna gigas* clam from the Geological Survey of Japan (Inoue et al., 2004); 2) a fragment of tropical coral *Siderastrea siderea* (BR-06) from the back reef of the southern Belize portion of the Mesoamerican Barrier Reef System (Chalk et al., 2021); 3) a fragment of deep-sea coral *Desmophyllum dianthus* (DY081-914DD) collected from the Labrador Sea (Standish et al., 2024); 4) a *Globigerinoides ruber* (sensu stricto, 300–355 μm) planktic foraminifera test (F8-2) from Ocean Drilling Programme (ODP) Site 999A (depth of 81–83 cm) in the western Caribbean (Schmidt et al., 2004); and 5) a fragment of coralline algae *Boreolithothamnion* cf. *soriferum* (CS9) from Loch Sween, Scotland (MacDonald et al., 2024).

A 5 mm thick slab was removed from a core of *Siderastrea siderea* BR-06 and divided into 80 mm sections using a diamond-tipped tile saw, then individual sections were polished using a diamond plate grinder followed by silicon carbide (SiC) grinding paper (Chalk et al., 2021). A small (~50 mm^2) area of the uppermost section, also analysed by Chalk et al. (2021), was then removed using a high carbon (HC) sintered diamond rotating saw. A whole "S1" septa of *Desmophyllum dianthus* DY081-914DD was sectioned using a HC sintered diamond rotating saw before its surface was decontaminated using SiC fixed abrasive P1200 grit papers (Standish et al., 2024). These two coral samples, as well as *Globigerinoides ruber* F8–2 and fragments of silicate reference materials NIST SRM610 and NIST SRM612, were separately mounted in MetPrep EpoFLO high purity, low viscosity, clear epoxy resin pucks (2.5 cm in diameter). With respect to BR-06, care was taken to ensure all pore spaces were fully impregnated with resin. The mounted samples were ground using a HC sintered diamond rotating grinder to either expose their surfaces (corals) or reveal the sample in section (foraminifera). Fixed abrasive P1200 SiC grit paper was used to prepare the surfaces for polishing, then polishing was performed using Kemet PSU-M polishing cloths (15 μm, 9 μm, and 3 μm grades) with diamond in oil suspension, before a final polish was carried out using Al_2O_3 0.3 μm with water. After polishing, samples were cleaned by ultrasonication in alcohol followed by 18.2 MΩ cm (ultrapure) water for 5 min. A single branch of *Boreolithothamnion* cf. *soriferum* CS9 was mounted in Buehler EpoThin resin, then was polished to reveal a transverse section. The sample was cleaned in a solution of 1 % H_2O_2 and 0.1 M NH_4OH for 20 h before being ultrasonicated for 5 min and rinsed three times in ultrapure water to remove surficial organic material. For images of the mounted samples, see Supplementary Fig. S1.

Pressed nanopowder pellets of carbonate reference materials JCp-1 and JCt-1 were produced in-house (Supplementary Fig. S1). Aliquots of micropowder (1.5 g) were milled with ultrapure water (8 g) in a Fritsch planetary ball mill at 600 Hz using 45 ml agate vials and 32 g of 5 mm agate balls. Milling consisted of 10 × 3-min cycles at 900 rpm, with 2-min pauses between each cycle. The resulting slurry was dried overnight at c.50 °C, re-homogenised using an agate hand pestle and mortar, and stored in acid-cleaned glass vials. Prior to milling a new reference material, the mill was cleaned/conditioned by twice completing the full milling procedure using pure calcium carbonate

powder (Thermo Scientific Alfa Aesar, LOT: Q09G066). The resulting slurry was disposed of each time. The pestle and mortar was ultrasonicated in ultrapure water for 5 min, then rinsed 3 times in ultrapure water, wiped with isopropanol alcohol, and dried using compressed nitrogen gas between each use. Nanopowder pellets, 10 mm in diameter, were produced using a manual hydraulic press (Specac, Orpington, UK) and a stainless-steel pellet die. Approximately 120 mg of powder was pressed at 5 MPa for 5 min. Between presses of different materials, the pellet die was cleaned by ultrasonication in ultrapure water for 5 min followed by 3× rinses in ultrapure water, wiped with isopropanol alcohol, then dried using compressed nitrogen gas. The pellets were mounted in recesses drilled into 2.5 cm diameter epoxy resin (MetPrep EpoFLO) pucks. They were secured using double-sided tape so that the pellet surfaces were flush with the surface of the resin mounts.

2.2. LA-TOF-ICP-MS

Elemental imaging was performed using a Nu Instruments (Nu Instruments Ltd., Wrexham, UK) Vitesse TOF-ICP mass spectrometer coupled to an Elemental Scientific Lasers (Bozeman, MT, USA) imageGEO193 laser ablation system with a TwoVol3 ablation chamber and Dual Concentric Injector. The instrumental set-up permits fast quasi-simultaneous detection across almost the entire elemental mass range (20–260 *m/z*) at a rate of 2.13 ms per baseline-corrected combined spectra, where each combined spectra consists of 80 individual spectra, or "accumulations" (see Supplementary Figs. S2, S3, and S4 for examples of chromatograms and a typical average spectrum). Two forms of corrections are accounted for: 1) gas blanks which are collected at the beginning of every other ablation line for the time elapsed between acquisition starting and the laser firing (typically about one second), and 2) electronic background, which is used to correct for the electronic noise within the system. The electronic background for each ion is determined for every individual integrated mass every 2 raw spectra (~50 μs) based on the noise over two 0.2 amu windows located a quarter mass above and a quarter mass below the intended mass. Ion detection employs a MangneTOF detector by ETP Electron Multipliers (Adaptas Solutions, Clyde, Australia), a sub-nanosecond TOF-specific device that is linear up to ~10,000,000 cps (equivalent to >1 V). Dark courts are ≤20 per minute at 3000 V.

Instrumental tuning was performed while ablating NIST SRM612, a silicate glass reference material, to achieve high sensitivity across the full mass range whilst minimising laser-induced elemental fractionation ($^{238}U^{+}/^{232}Th^{+} \approx 1$). General operating conditions are detailed in Table 1. Operation with relatively high He and H_2 gas flows (Table 1) in the mass spectrometer's always-on collision reaction cell (CRC) suppresses the Ar signal and helps to break down any oxides or other polyatomic interferences (Lockwood et al., 2024). The analysed mass range can be controlled using the Vitesse's Bradbury-Nielsen gate, a device more commonly known as an "ion blanker" (Lockwood et al., 2024). For all sequences, the mass range from 27.3 to 40.6 *m/z* was blanked out to prevent detector saturation from ^{28}Si (silicate glasses) and ^{40}Ca (carbonates). In addition, the following mass ranges were also blanked out during certain analytical sequences, also to prevent detector saturation: 40.6–44.6 (^{44}Ca) and 86.7–99.0 (^{88}Sr) when analysing BR-06; 40.6–44.6 (^{44}Ca), 49.5–58 (^{56}Fe), and 86.7–99.0 (^{88}Sr) when analysing F8–2; and 86.7–99.0 (^{88}Sr) when analysing CS9. The laser ablation system was operated in imaging mode to account for acceleration and deceleration of stages which would otherwise show as artefacts in images as irregularly spaced shots at the beginning and end of each line.

Signal intensity data for the following isotopes were typically exported for data reduction, with only those present at detectable levels within each sample taken forward for further reporting: ^{23}Na, ^{24}Mg, ^{27}Al, ^{30}Si, ^{31}P, ^{43}Ca, ^{44}Ca, ^{46}Ca, ^{48}Ca, ^{51}V, ^{52}Cr, ^{55}Mn, ^{56}Fe, ^{59}Co, ^{60}Ni, ^{63}Cu, ^{66}Zn, ^{85}Rb, ^{86}Sr, ^{88}Sr, ^{89}Y, ^{90}Zr, ^{133}Cs, ^{138}Ba, ^{139}La, ^{140}Ce, ^{141}Pr, ^{146}Nd, ^{149}Sm, ^{153}Eu, ^{157}Gd, ^{159}Tb, ^{163}Dy, ^{165}Ho, ^{166}Er, ^{169}Tm, ^{172}Yb, ^{175}Lu, ^{178}Hf, ^{208}Pb, ^{232}Th, and ^{238}U. Data reduction was performed in Iolite 4 using the Trace_Elements data reduction scheme (DRS: Paton et al., 2011). The geometry of some of the samples resulted in the laser ablation patterns being placed overlying both sample and surrounding epoxy resin, resulting in the analyses of both. Therefore, to isolate only those spectra corresponding to measurement of calcium carbonate, a total (integrated) signal threshold of 500,000 counts per second (cps) was invoked in the DRS prior to data reduction (Fig. 1). This value was determined following a thresholding test, where it was found that pixels relating to the resin were still common when using a total beam threshold value of 250,000 cps (Fig. 1C) whilst sections of the sample carbonate, i.e. the target of analysis, were lost when using a total beam threshold value of 750,000 cps (Fig. 1E). Thus, whilst there is some flexibility in the total beam thresholding value used (values ranging from ~300,000 to ~700,000 are likely to be appropriate), a value of 500,000 cps was deemed suitable for the cases presented here.

Two strategies were then employed. In the first, intensities (in cps) were internally normalised to ^{48}Ca based on the expected Ca concentrations of the material analysed and externally normalised to repeat analyses of a pressed nanopellet of the matrix-matched carbonate reference material JCp-1 (i.e. single-point calibration), a *Porites* sp. coral. The expected Ca concentration employed was 40 % (based on the typical composition of calcium carbonate) except for cases where literature data indicates otherwise: BR-06 used a value of 38.5 % based on characterisation of tropical coral *Porites* sp. (Aizawa, 2008; Okai et al., 2002) and CS9 used a value of 35.7 % based on analyses of coralline algae (Smith et al., 2012). Drift in the intensities of the reference material were smoothed with a spline function ("Spline_Smooth 1"), and the concentrations reported by Jochum et al. (2019) were used in the external normalisation calculations (specifically, the mean values of unmilled powder reported in their Table 2c). In the second strategy, intensities were only externally normalised to JCp-1, as above. The latter strategy was explored for situations where the expected Ca concentration required for internal normalisation cannot be reasonably ascertained (e.g. when ablating high-Mg carbonates). Measurement of JCp-1 consisted of pairs of ~3 s line analyses repeated every ~30 min throughout the analytical sequence. Fig. 2 shows a timeseries of paired JCp-1 and JCt-1 analyses from a typical analytical sequence, demonstrating instrument stability across a 9.5 h period.

Table 1
Operating conditions for LA-TOF-ICP-MS.

Instrument	
Mass Spectrometer	Nu Instruments Vitesse time of flight inductively coupled plasma mass spectrometer
Laser Ablation System	Elemental Scientific Lasers imageGEO193 laser ablation system with a TwoVol3 ablation chamber
RF Power	1350 W
Cones	Ni sample cone (319–646), Ni skimmer cone (325–294)

Gas Flows		Ablation Conditions	
Cool Gas (Ar)	13 l min^{-1}	Laser energy density	~3.0 J cm^{-2}
Auxiliary Gas (Ar)	2 l min^{-1}	Laser repetition rate	200–400 Hz
Make-up gas (Ar)	0.825 l min^{-1}	Laser beam shape	Square
Cell (CRC) Gas 1 (He)	0.016 l min^{-1}	Laser beam width	1 or 2 μm
Cell (CRC) Gas 2 (H_2)	0.008 l min^{-1}	Laser tracking speed	200 μm s^{-1}
Ablation chamber carrier gas (He)	0.2 l min^{-1}	Spacing	0.75–1 μm
Ablation cup gas (He)	0.3 l min^{-1}	Ablation mode	Line
Additional Gas (N_2)	0.002 l min^{-1}		

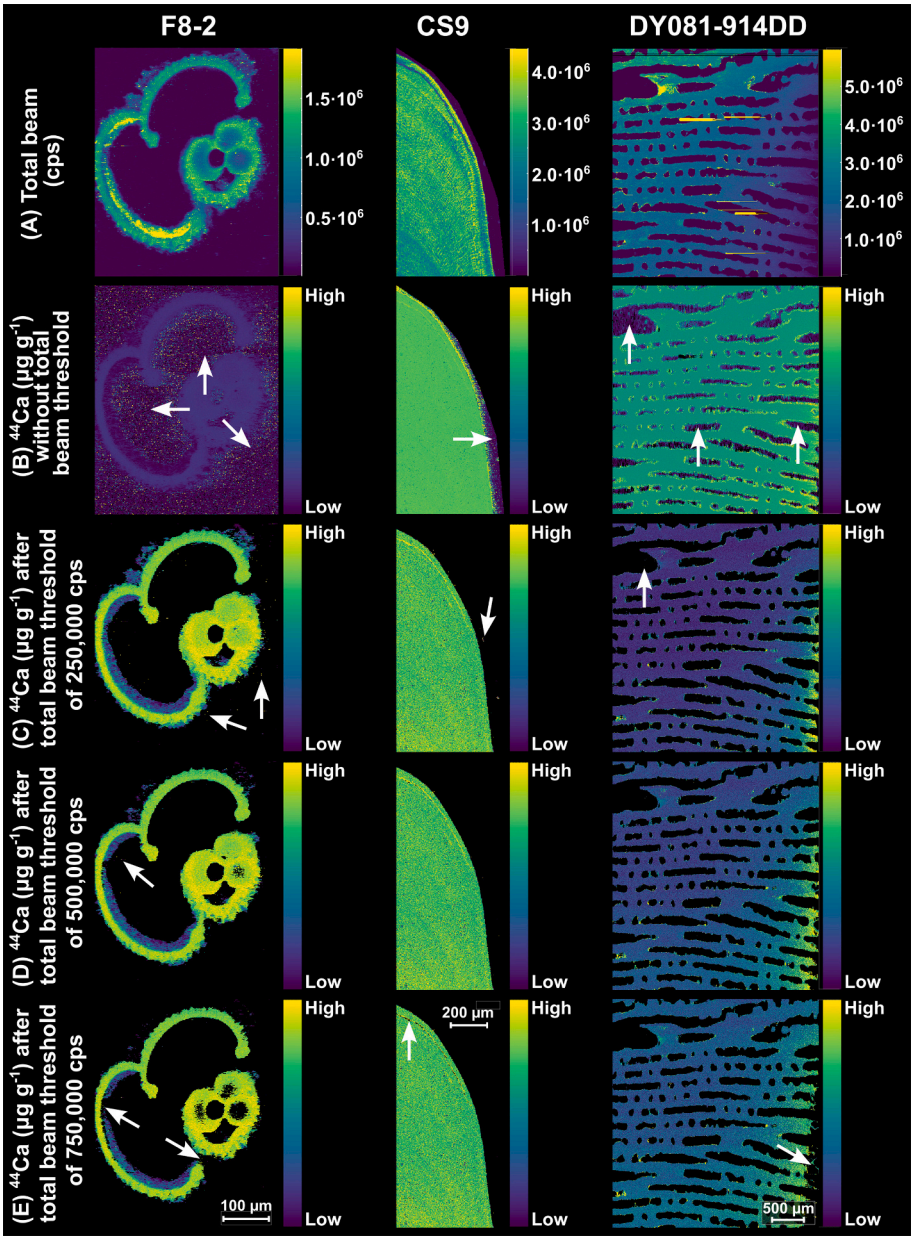

Fig. 1. Examples of thresholding using the total ion beam signal (A) in Iolite to isolate pixels relating only to the carbonate samples (*Globigerinoides ruber* (sensu stricto) F8–2, *Boreolithothamnion* cf. *soriferum* CS9, *Siderastrea siderea* BR-06) under investigation (B–E). When thresholding is not performed (B), the images contain pixels relating to analysis of the resin used to mount the samples; when thresholding uses a total beam value of 250,000 cps (C), resin pixels are still common; when thresholding uses a total beam value of 500,000 cps (D), resin pixels are very rare; and when thresholding uses a total beam value of 750,000 cps (E), sections of the sample carbonate, i.e. the target of analysis, are lost. This study therefore thresholds using a total beam signal of 500,000 cps.

2.3. Solution ICP-MS

To provide comparative data for the imaged *Globigerinoides ruber* (F8–2), further foraminiferal tests from ODP Site 999 A (sensu stricto, depth of 81–83 cm, 300–355 µm size fraction) were picked and characterised for element/calcium ratios (E/Ca) by solution ICP-MS approaches. Four samples were processed, each consisting of ~30–40 tests and equating to ~300–400 µg of material. Tests were cracked between two glass slides under a microscope, and any contaminating clays were removed by ultrasonication in ultrapure water. They subsequently underwent oxidative cleaning procedures (Barker et al., 2003). After dissolution in ~0.15 M Teflon-distilled HNO_3, elemental analyses were performed on an Element XR High Resolution single collector ICP mass spectrometer (Thermo Fisher Scientific, Waltham, MA, USA) following established methods (Henehan et al., 2015). Total acquisition time for each sample was 123 s. Reproducibility of element ratio measurements was optimised by matrix-matching samples and their bracketing in-house gravimetric standards (Henehan et al., 2015). Internal consistency standards were analysed throughout every analytical session to monitor reproducibility and accuracy of element ratios. Analytical reproducibility is better than ±5 % (2 SD) for Li/Ca, B/Ca, Na/Ca, Mg/Ca, Mn/Ca, Sr/Ca, Cd/Ca, Ba/Ca, Nd/Ca, and U/Ca, and better than ±30 % (2SD) for Al/Ca and Fe/Ca.

3. Results and discussion

3.1. Accuracy and limits of quantification

Sensitivity of the instrumental set-up was determined based on analyses of both NIST SRM612 silicate glass and JCp-1 pressed nanopellet,

Table 2
Summary of LA-TOF-ICP-MS analyses of marine carbonates BR-06 (*Siderastrea siderea*), DY081-914DD (*Desmophyllum dianthus*), F8–2 (*Globigerinoides ruber*), and CS9 (*Boreolithothamnion* cf. *soriferum*), compared to data collected through other analytical techniques.

Sample ID	E/Ca[a]	Solution ICP-MS		LA-ICP-MS				LA-ToF-ICP-MS (this study)		
		Mean ± SD	Ref[b]	Mean ± SD	CV	Skew[X]	Ref[b]	Mean ± SD	CV	Skew[X]
DY081-914DD	Mg/Ca	2.2 ± 0.1	1	2.4 ± 0.5	0.2	0.0	3	1.6 ± 0.6	0.4	11.6
	Sr/Ca	10.60 ± 0.03	1	10.3 ± 0.4	0.0	0.4	3	9.6 ± 0.6	0.1	0.3
	Ba/Ca	8.3 ± 0.3	2	9 ± 0.7	0.1	0.3	3	7.5 ± 6.3	0.8	398.6
	U/Ca	1939.8 ± 75.3	3	1715.6 ± 497.6	0.3	0.7	3	1634.7 ± 1076.9	0.7	0.9
BR-06	Mg/Ca	3.7 ± 0.1	4	4.1 ± 0.6	0.1	9.5	5	3.5 ± 1.2	0.3	86.8
	Sr/Ca	8.51 ± 0.03	4	8.4 ± 0.9	0.1	0.8	5	10.5 ± 2.7	0.3	80.5
	Ba/Ca	–	–	14.3 ± 7.5	0.5	9.2	5	93.8 ± 5050.8	53.9	102.4
CS9	Mg/Ca	–	–	195.5 ± 38.2	0.2	0.6	6	218.2 ± 52.1	0.2	0.1
	Sr/Ca	–	–	3.2 ± 0.5	0.2	2.9	6	3.6 ± 0.7	0.2	7.1
	Ba/Ca	–	–	5.9 ± 2.9	0.5	75.8	6	15.4 ± 155.0	10.1	148.0
F8–2	Mg/Ca	4.0 ± 0.1	–	–	–	–	–	3.2 ± 1.7	0.5	81.6
	Sr/Ca	1.40 ± 0.01	–	–	–	–	–	1.3 ± 0.4	0.3	71.2
	Ba/Ca	1.15 ± 0.08	–	–	–	–	–	1044.0 ± 132,784.1	127.2	167.6

[a]Mg/Ca and Sr/Ca in mmol/mol, Ba/Ca in μmol/mol, U/Ca in nmol/mol. [b]Ref. = Reference, where 1 is Stewart et al. (2016), 2 is Kershaw et al. (2023), 3 is Standish et al. (2024), 4 is Fowell et al. (2016), 5 is Chalk et al. (2021), 6 is MacDonald et al. (2024).

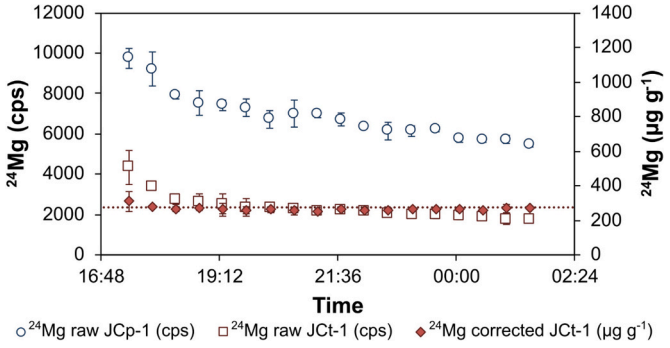

Fig. 2. Timeseries (^{24}Mg) of JCp-1 and JCt-1 analyses from a typical analytical sequence, demonstrating instrument stability across a 9.5 h period (2SD of the corrected JCt-1 measurements is <10 %). Each data symbol represents the mean (±2SE) of a pair of consecutive measurements. JCt-1 are normalised to JCp-1 following the protocol detailed in Section 2.2. The dashed red line represents the reference Mg concentration of JCt-1 from Jochum et al. (2019), which agrees well with the corrected JCt-1 concentrations from the present study. (For interpretation of the references to colour in this figure legend, the reader is referred to the web version of this article.)

using a 1 by 1 μm square laser beam and with all other laser parameters the same as detailed in Table 1. Both materials show increasing sensitivities at high *m/z*, and have broadly similar sensitivity ranges from ~10^1 cps/μg g^{-1} at low m/z to ~10^3 at the high m/z (Fig. 3).

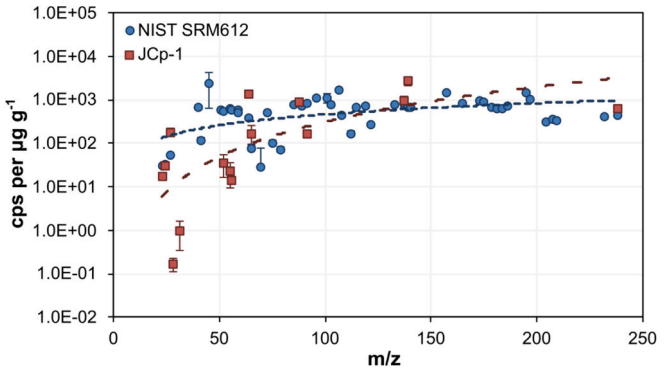

Fig. 3. cps per μg g^{-1} (corrected for isotope abundance) versus m/z for analyses of NIST SRM612 silicate glass and JCp-1 pressed carbonate nanopellet, along with power law trendlines for each dataset. Only those elements within the limits of quantification (LoQ), calculated below, are shown.

Accuracy is determined by comparing the analyses of JCt-1 carbonate nanopellet with a 1 by 1 μm square laser beam (Supplementary Figs. S5 and S6) to the micropellet data published by Jochum et al. (2019), after data reduction following the strategies detailed above. With both internal normalisation to ^{48}Ca and external normalisation to repeat analyses of JCp-1, and based on the average of 500 laser ablation lines (total acquisition time 13.8 min), mean accuracy is <7 % when elemental concentrations are >0.5 μg g^{-1} (based on the analyses of nine elements: Fig. 4A and Fig. 4B). The lower limit of quantification (LoQ) is therefore proposed to be 0.5 μg g^{-1}, although in some instances analyses of elements with lower concentrations are deemed to be accurate, e.g. Cr (accuracy to 7 % by LA-TOF-ICP-MS, with a concentration of 0.467 μg g^{-1} reported by Jochum et al., 2019). Accuracy and LoQ are similar when internal normalisation is not performed, providing data are externally normalised to a matrix matched reference material — which in this case was JCp-1 (Fig. 4). Irrespective of this, all samples presented in Section 3.2. below are normalised both internally and externally, as this is considered the more thorough approach.

The instrument detector trips, and an ion blanker is automatically inserted around the mass in question, when signal intensities exceed ~10 million cps for a few milliseconds; this defines the upper LoQ. Based on instrumental sensitivity determined in Fig. 3, the maximum concentrations that can be measured range from ~30 % at the low mass range to ~0.15 % at the high mass range, assuming an isotopic abundance of 100 % for a particular element.

Two standard deviations of 500–1.6 s transects of JCt-1 is <10 % for elements present at >100 μg g^{-1}, and < 45 % for elements present at between the LoQ and 100 μg g^{-1} (Fig. 4C). Assuming homogeneity of the JCt-1 nanopellet (see below, and also Boer et al., 2022; Jochum et al., 2019; Nambiar et al., 2024), these values constrain the precision of single laser ablation transect and indicates only elements present at >100 μg g^{-1} will be accurately measured to better than 10 % for any given single transect. Two standard deviations of 332 repeat ~4 ms spectra for individual pixels of JCt-1 is below ~150 % for elements present at >100 μg g^{-1}, and below ~1000 % for elements present at between the LoQ and 100 μg g^{-1} (Fig. 4D). This constrains the precision of individual data cycles which constitutes a single pixel, again assuming JCt-1 is homogeneous at this level. The best pixel-level precision is recorded for Na and Sr, the only two elements that are present in concentrations of >1000 μg g^{-1} in JCt-1 (other than Ca), which are ≤30 % and ≤ 15 % respectively when data are internally normalised to ^{48}Ca.

3.2. Marine carbonate case studies

3.2.1. Comparisons with other techniques and assessments of variability

To demonstrate the viability of our ≤2 μm width pixel geochemical

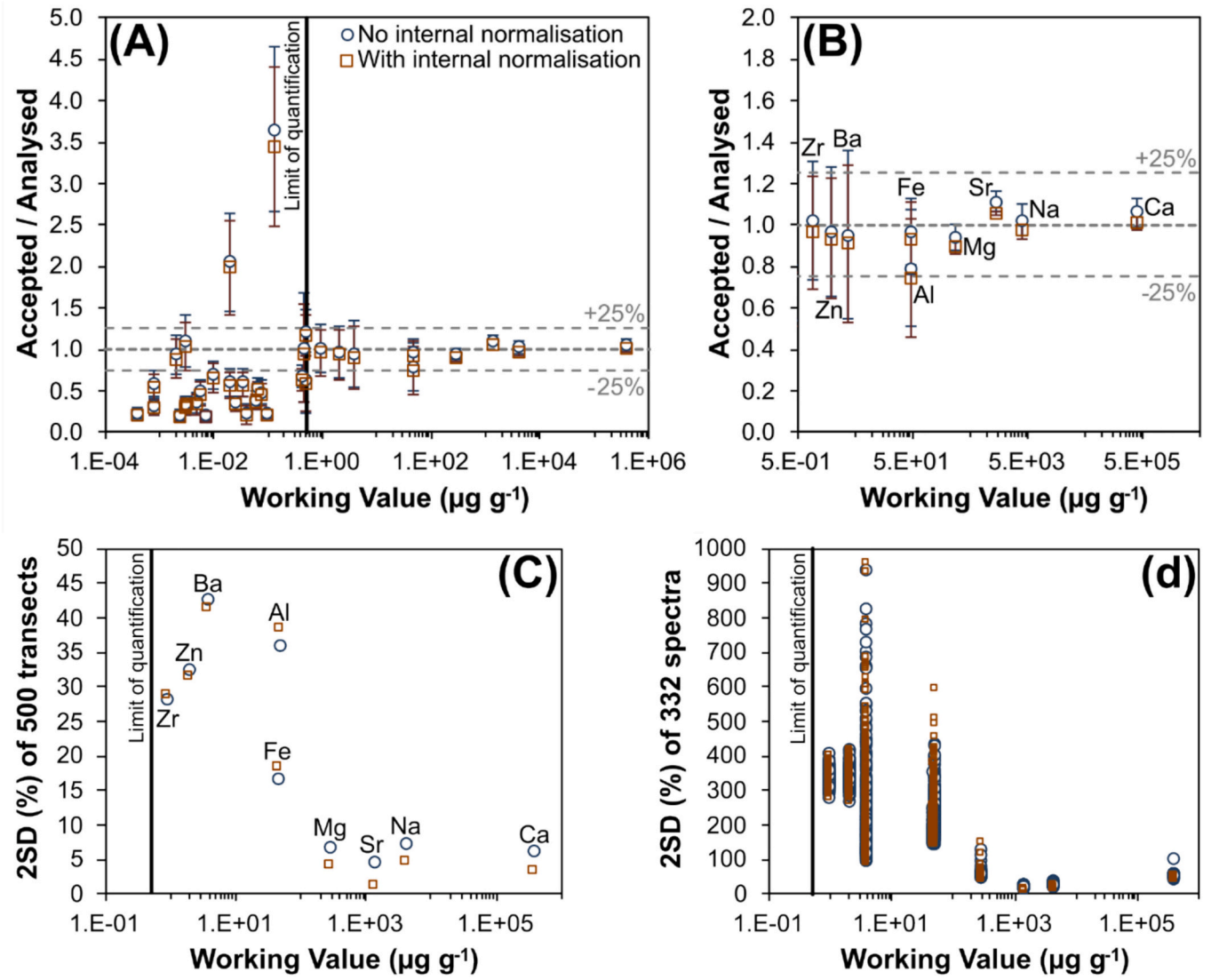

Fig. 4. Accuracy and reproducibility of LA-TOF-ICP-MS analytical approach based on analysis of JCt-1. (A) and (B): Accuracy based on the mean (±2 SD) of 500 laser ablation transects of JCt-1, where (A) shows all elements and (B) shows only those present in JCt-1 above the lower LoQ. (C) Reproducibility (2SD %) of 500 transects of JCt-1 for selected elements with working values above the lower LoQ. (D) Reproducibility (2SD %) of 332 spectra of JCt-1 for the same selected elements. All data are externally normalised to JCp-1 but are shown both with (red squares) and without (blue circles) internal normalisation to ^{48}Ca. Lower limit of quantification of 0.5 µg g^{-1} is marked on (A), (C), and (D) as a solid black line. Working values are from Jochum et al. (2019). (For interpretation of the references to colour in this figure legend, the reader is referred to the web version of this article.)

imaging approach to marine carbonates, 2D images from four samples have been collected: a fragment of deep-sea coral *Desmophyllum dianthus* skeleton (DY081-914DD), a fragment of tropical coral *Siderastrea siderea* skeleton (BR-06), a *Globigerinoides ruber* (sensu stricto) planktic foraminifera test (F8–2), and a fragment of coralline algae *Boreolithothamnion* cf. *soriferum* skeleton (CS9). All have previously been analysed by alternative techniques (solution ICP-MS or traditional LA-ICP-MS using either a Thermo Scientific X-Series II Quadrupole ICP mass spectrometer or Agilent 8900 Triple Quadrupole ICP mass spectrometer coupled to an NWR193 laser with TwoVol2), and comparisons of selected E/Ca are provided in Fig. 5 and Table 2 (see also Supplementary Fig. S7). Note that in all instances, TOF analyses were not performed on the exact skeletal region or test that had previously been analysed, thus datasets are considered as a general guide to accuracy of the TOF approach only (see Supplementary Table S1 for further details).

Overall agreement is good, with LA-TOF-ICP-MS analyses being consistent with solution ICP-MS and/or traditional LA-ICP-MS; mean TOF analyses of each of the selected E/Ca fall within 1SD of the comparative dataset in all cases except the Sr/Ca of DY081-914DD, where it is within 2SD. The coefficient of variation (CV) is a measure of relative variability and is expressed as the population standard deviation divided by the population mean. CV is greater in the TOF data compared to the traditional LA-ICP-MS datasets for all samples and E/Ca where comparative data exists (Table 2). This difference is most obvious for the tropical coral BR-06, where the CV of the TOF data is always at least double that of the traditional LA-ICP-MS data, and for the Ba/Ca of all samples where the CV of TOF data is at least x10 that of traditional LA-ICP-MS data. Likewise, the CV of the TOF data for foraminifera F8–2 is larger than that of solution ICP-MS dataset for all ratios. The greater variation recorded by LA-TOF-ICP-MS compared to traditional LA and solution approaches is best explained by the higher analytical resolution of the former (1–2 µm pixel widths); solution data is based on bulk analyses (~300–400 µg of sample for foraminifera, a few mg of sample for coral) whilst LA-ICP-MS data was collected using either a square laser beam with a width of 25 µm (DY081-914DD), a circular laser beam with a diameter of 50 µm (CS9), or a rectangular laser beam 140 by 50 µm in

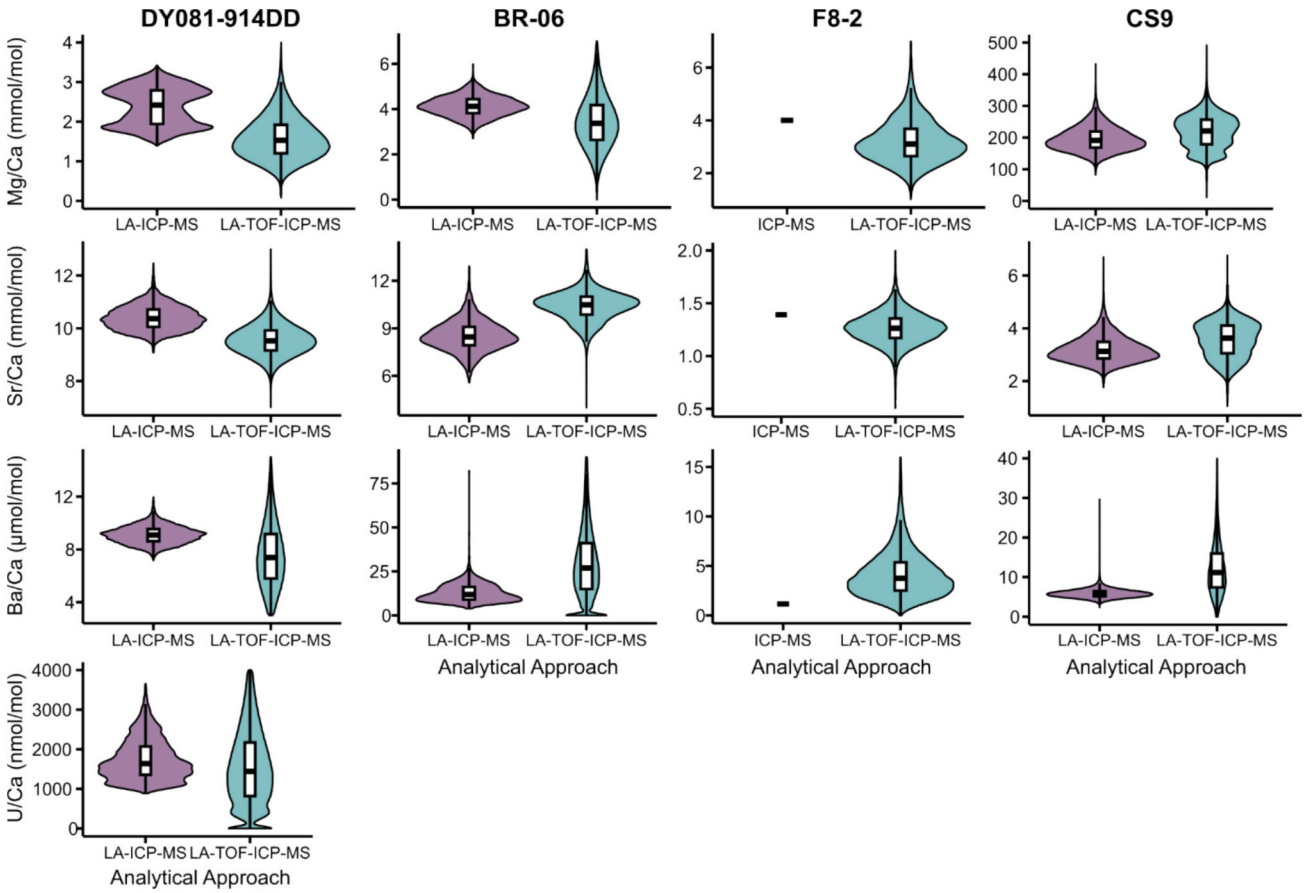

Fig. 5. Comparison of LA-TOF-ICP-MS analyses to data collected using alterative analytical techniques for the four samples *Siderastrea siderea* BR-06, *Desmophyllum dianthus* DY081-914DD, *Globigerinoides ruber* (sensu stricto) F8–2, and *Boreolithothamnion* cf. *soriferum* CS9. Note that for ICP-MS analysis of F8–2, only the average value is shown due to the low number of repeat measurements ($n = 4$).

size (BR-06). With respect to Ba/Ca, both the higher mean (93.8 µmol/mol) and greater variation (CV = 53.9) of BR-06 analysed by TOF also relates to the fact that the region analysed was the top-most portion of the skeleton that incorporates the tissue layer from the time it was sampled. The Ba/Ca of coral skeletons is known to be influenced by organic- rather than carbonate-bound Ba (Serrato Marks et al., 2017; Sinclair et al., 1998), and such enrichments are typically found in the outer layers of coral skeletons. Similarly, the higher mean and greater variation of Ba/Ca for F8–2 likely relates to silicate, organic, and/or Fe-Mn oxyhydroxide contamination (Barker et al., 2003). The approaches used for screening data impacted by contamination are detailed sample by sample below.

The D'Agostino test for skewness (D'Agostino, 1970), a measure of the asymmetry of a distribution, was performed on all datasets using the 'skewness' function in R ('moments' package: Komsta and Novomestky, 2015). All TOF datasets are characterised by positive skewness values (Table 2) and can be classified as highly skewed (values >1) except for U/Ca of DY081-914DD which is moderately skewed (values of 0.5–1), and Mg/Ca of CS9 and Sr/Ca of DY081-914DD which are approximately symmetric (values <0.5). Skewness values for the TOF datasets are typically greater than those of traditional LA-ICP-MS datasets, although the latter are also characterised by positive values barring the exception of DY081-914DD Mg/Ca, indicating tailing towards higher values is the norm. Greater skewness of the TOF data again likely relates to the higher spatial resolution of the TOF analyses that is capable of isolating sample regions with higher elemental concentrations relative to Ca that are otherwise supressed at lower resolution. Like CV, skewness values are typically larger for the tropical coral BR-06 than any other sample, and for Ba/Ca than any other E/Ca. With respect to Ba/Ca, this may again relate to the variable presence of organic-bound Ba (Serrato Marks et al., 2017; Sinclair et al., 1998).

Overall, this comparison shows that our 1–2 µm pixel 2D images collected by LA-TOF-ICP-MS compare well with previous studies. However, the higher spatial resolution we achieve reveals considerably more variation in E/Ca than was hitherto recorded (Table 2). It is also notable that despite how unrelated the various taxa analysed here are, and the differences in absolute values, the degree of variability in Mg/Ca and Sr/Ca appears similar based on the coefficient of variation. Yet contrasting skewness reveals that there are taxa specific elemental distributions that most likely reflect the contrasting biomineralisation strategies employed by the species examined (Erez, 2003; Nash et al., 2019; Sun et al., 2020).

3.2.2. *Deep-sea coral Desmophyllum dianthus*

A 2 by 2 mm area of *Desmophyllum dianthus* DY081-914DD was imaged using a 2 by 2 µm laser beam with 1 µm spacing, tracking at a speed of 200 µm s^{-1}. These conditions were chosen to produce a high-resolution image in a reasonable timeframe. The resulting images show clear variation across the sampled area with several linear bands evident in a number of E/Ca ratios, including Na/Ca, Mg/Ca, Al/Ca, Sr/Ca, La/Ca and U/Ca (Fig. 6, see also Supplementary Fig. S8). Scleractinian coral skeletons are composed of two key structural components: centres of calcification (COCs), where nucleation of new skeleton begins, are the components that drive skeletal extension; while the fasciculi, composed of fibrous aragonite crystals, thicken the skeleton (Nothdurft and Webb, 2007). It is well accepted that these structures are characterised by contrasting geochemical compositions, for example COCs are relatively more enriched in Mg and depleted in U (Chen et al., 2021,

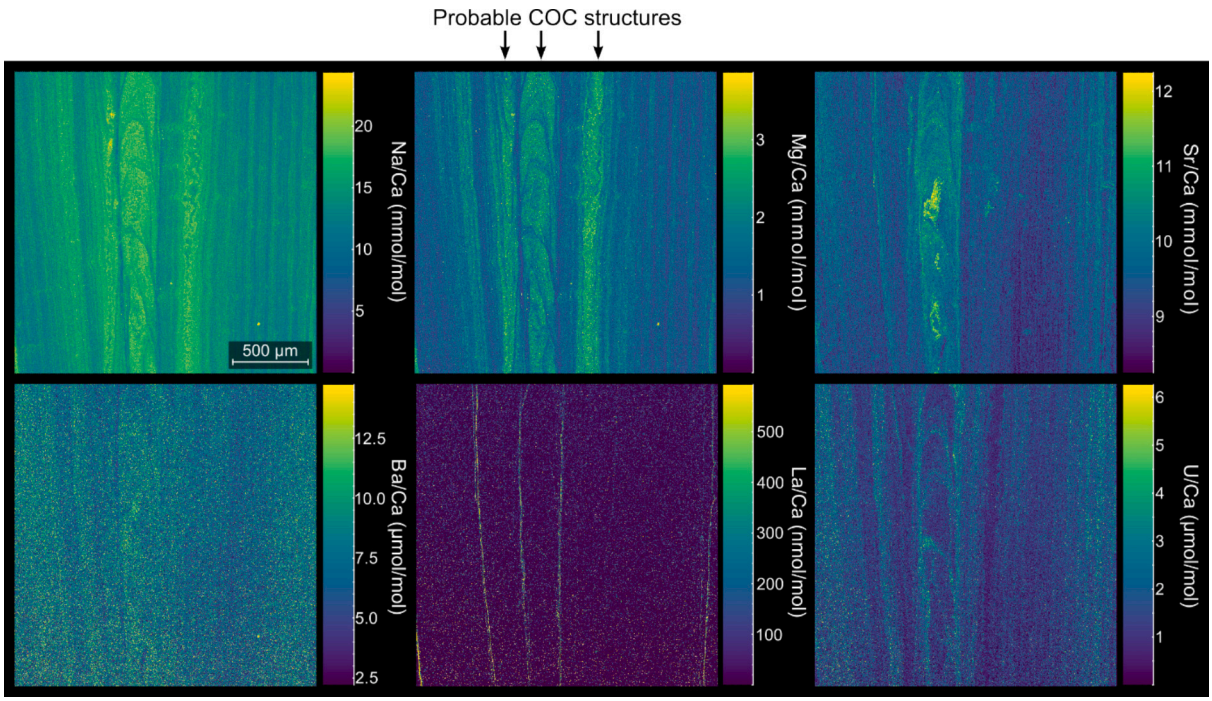

Fig. 6. Geochemical images of deep-sea coral *Desmophyllum dianthus* skeleton DY081-914DD. No filters were applied to these images in Iolite.

2023; Gagnon et al., 2007; Meibom et al., 2004; Robinson et al., 2006; Sinclair et al., 2006). With respect to DY081-914DD, this was recently demonstrated using a correlative multimodal imaging approach (Standish et al., 2024). Thus, the vertical linear features with higher Mg/Ca and lower U/Ca depicted in the central portion of the images in Fig. 6 are best explained as being primary or secondary COCs, but these are imaged here at >10 times the resolution than in Standish et al. (2024) and so are shown with a far greater level of structural detail (cf. Fig. 2 in Standish et al., 2024, which was produced using a 25 µm wide square laser beam). The suite of images in Fig. 6 indicates that the COCs are also characterised by higher Na/Ca and Sr/Ca, adding to our understanding of structurally-driven geochemical variation within coral skeletons. It has previously been noted that such variation has the potential to complicate the results of studies concerned with geochemical proxy development and application if unknown proportions of these structures are sampled from the coral skeleton, (Chalk et al., 2021; DeLong et al., 2016; Standish et al., 2024; Stewart et al., 2016), and it is worth reiterating this point here.

Mg ions are an important component of amorphous calcium carbonate (ACC), aiding its formation and stability (Addadi et al., 2003; Politi et al., 2010). Recent models of calcium carbonate biomineralisation in a wide range of marine calcifiers have favoured an ACC precursor phase that forms in vesicles of intracellular calcifying fluid before attaching to the biomineral growth front (Gilbert et al., 2022; Sun et al., 2020), thus the distribution of Mg within coral skeleton can indicate skeletal regions where particle attachment likely plays a greater role in biomineralisation, and this is a key piece of evidence in proposals that argue particle attachment as the dominant mechanism in the formation of COCs (Standish et al., 2024). However, the high-resolution imaging achievable by TOF-MS, and presented in Fig. 6, moves beyond the broad high-Mg and COC association, and documents substantial Mg variations within the COCs and regular banding in the fibrous components that surround them.

A key benefit of the LA-TOF-ICP-MS approach is that data are collected simultaneously for a majority portion of the mass range (20–260 *m/z*), and unlike traditional LA-ICP-MS (e.g. quadrupole or triple quadrupole ICP-MS) there is no need to pre-determine which elements will be studied or balance the advantages of larger elemental suites with the disadvantages of increased analysis time. This results in the collection of data for elements that otherwise would not have been included, for example here the rare earth element (REE) La (and other elements such as Y) shows distinct highs on the boundary of some of the secondary COC features. Further investigation is required to determine exactly what these features are, but one possibility is that they are linear voids filled with a REE-enriched contamination phase. Fe-Mn oxyhydroxides forming on the seafloor are common contaminants of REE's in deep sea corals (Flierdt et al., 2010), however neither Mn or Fe (nor Th, a common indicator of Fe-Mn oxyhydroxide contamination) are enriched in these features, potentially documenting the existence of additional sources of contamination in deep sea corals that may not be removed by current cleaning protocols (Flierdt et al., 2010). Further investigation into understanding the causes of these features is therefore warranted.

3.2.3. *Tropical coral Siderastrea siderea*

A 3.2 by 3.6 mm area of tropical coral *Siderastrea siderea* BR-06 was imaged using a 2 by 2 µm square laser beam with 1 µm spacing, tracking at a speed of 200 µm s^{-1} (Fig. 7, see also Supplementary Fig. S9 for a full suite of elements). Unlike *Desmophyllum dianthus* DY081-914DD, the skeleton of BR-06 is porous with much smaller skeletal microstructural components, and although ablation encompassed the entire 3.2 by 3.6 mm area, pixels relating to the resin-filled pore spaces were masked out during data processing (using a total beam cut-off of 500,000 cps in the DRS). Despite the more challenging scale, small ~25 µm-wide features characterised by high Na/Ca and Mg/Ca are clearly visible running broadly horizontal on the images in Fig. 7 (~parallel to the growth axis) in almost all the skeletal components, and we interpret these as being COCs, which are known to be smaller in tropical corals than in deep sea corals like DY081-914DD. Such features were not visible in previous work on this species that used traditional LA-ICP-MS approaches and a circular laser beam 140 µm in diameter (Chalk et al., 2021), highlighting the benefits of the high-resolution TOF approach.

Previous work has highlighted the existence of compositional variation between the columella, the centre of each corallite, and the thecal walls that form the boundaries of each corallite (Chalk et al., 2021). Consistent with this work, we find that Mg/Ca on average is lower in the

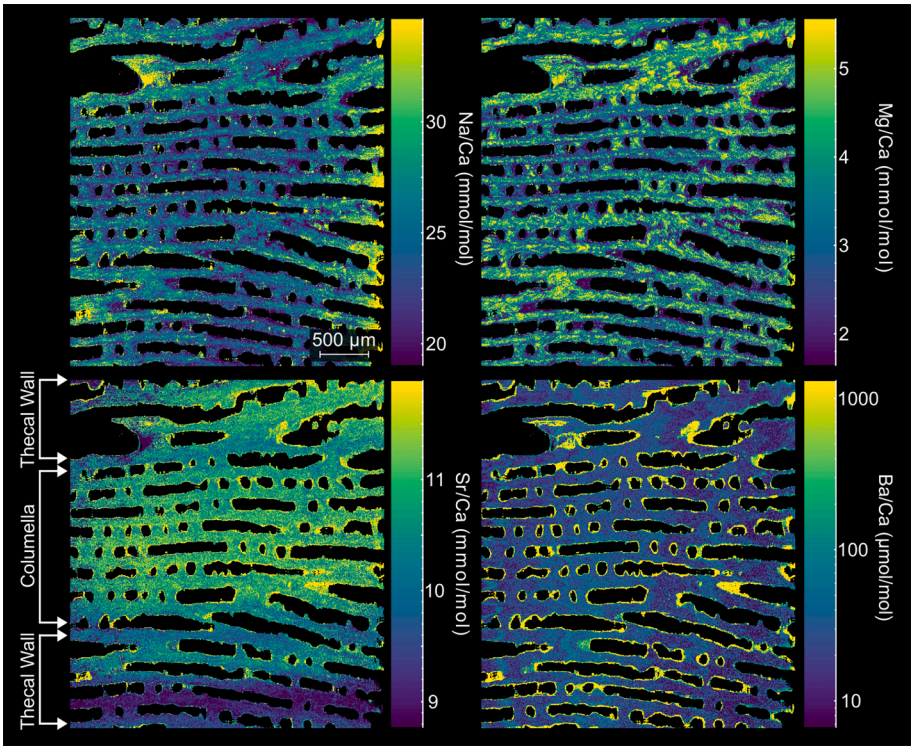

Fig. 7. Geochemical images of tropical coral *Siderastrea siderea* skeleton BR-06. Note colour scale for Ba/Ca is logarithmic rather than linear. Iolite filters applied: 'masks' on intermediate channels Mg24/Ca48 (>0.08) and Fe56 (>50,000 cps), and output channel Sr86 (<2000 µg g^{-1}), to screen pixels within the pore spaces for improved clarity, and 'replace null'. Direction of coral growth is from left to right.

columella portion of the skeleton of BR-06 (Chalk et al., 2021). Conversely, Sr/Ca is shown to be higher in the columella, and although this was not recorded previously in BR-06 by LA-ICP-MS (Chalk et al., 2021), it is consistent with previous work on this species (DeLong et al., 2016). With Sr/Ca being a key seawater temperature proxy, such structural variations again highlight the need for consistent sampling of the coral skeleton when studies are concerned with geochemical proxies.

As discussed previously, the Ba/Ca of BR-06 is highly variable, and Fig. 7 shows that this is largely driven by high Ba in the skeleton immediately surrounding the pore spaces. It would be expected for organic-bound Ba associated with the tissue layer to be focussed on the internal surfaces of the skeleton, thus this supports the notion that such high Ba/Ca regions are indeed associated with organics. Mg/Ca has also been used to identify skeletal regions influenced by organic matter in the past, whilst correlations between Ba/Ca and both Mg/Ca and Pb/Ca have been identified in other studies (Serrato Marks et al., 2017). The presence of organic-bound material is therefore likely the cause of the high CV and skewness values returned for this sample more generally, irrespective of E/Ca. Indeed, Fig. 7 shows that in some instances those regions surrounding the pores characterised by high Ba/Ca are also characterised by high Na/Ca and Sr/Ca. Whilst much of the variation in Ba/Ca appears to be driven by this organic contamination, further variation is apparent, for instance narrow bands perpendicular to the direction of growth are evident that may record discrete inputs of Ba to the Belize Barrier Reef, possibly relating to terrestrial run-off events (McCulloch et al., 2003; Shaw et al., 2024). Thin, ~1 µm-thick, features characterised by high Al and Fe are also visible within the skeleton running parallel to the growth direction and these appear to occur in the very centres of the high Mg/Ca COCs (Supplementary Fig. S9). However, we refrain from interpreting these further due to the use of Al_2O_3 during sample polishing, and although this is also seen in DY081-914DD (Supplementary Fig. S8) perhaps suggesting a common mechanism, further imaging on samples that have not been prepared with Al_2O_3 is required.

3.2.4. *Planktic foraminifera Globigerinoides ruber*

A 0.4 by 0.5 mm area encompassing *Globigerinoides ruber* test F8–2 was imaged using a 1 by 1 µm square laser beam with 0.75 µm spacing, tracking at a speed of 200 µm s^{-1} (Fig. 8, see also Supplementary Figs. S10 and S11). For bulk analysis of element composition, foraminiferal samples are typically cracked open, fragmented, and subjected to an extensive physical cleaning protocol aimed at removing silicate, organic and Fe-Mn oxyhydroxide contamination (Barker et al., 2003). The efficiency of detrital silicate removal is typically monitored through Al/Ca, and whether Fe-Mn oxyhydroxides have been removed is monitored through Mn/Ca (or Fe/Ca: Barker et al., 2003). For in situ analysis of foraminifera some studies also crack open the foraminifera (Spero et al., 2015) and clean the shell fragments in a similar way prior to analysis, but others do not because such fragmentation removes the ontogenic context of the analyses (Kearns et al., 2023). As a result, screening using Al/Ca and/or Mn/Ca or Fe/Ca is essential to ensure the foraminiferal carbonate is identified for further analysis. Here we apply a mask based on Al >80,000 cps to isolate the foraminiferal carbonate (Fig. 8), but see Supplementary Fig. S10 for unscreened images.

Previous studies focusing on 2D mapping of the elemental composition of foraminifera typically only image a segment of a single chamber (Bonnin et al., 2019; Fehrenbacher and Martin, 2014; John et al., 2023). While informative, this limits our understanding of trace element variability with respect to ontogeny. Here, due to the rapidity of data collection using the LA-TOF, we can image all the chambers in the final whorl, including some earlier chambers evident in the right of Fig. 8. This more complete view highlights that a number of elements appear to be lower concentration in the final and penultimate chambers than the earlier chambers (i.e. Mg/Ca, Na/Ca, Sr/Ca, Ce/Ca, La/Ca, Ba/Ca; Fig. 8). For Mg/Ca in *Globigerinoides ruber* at least, this has already been seen in previous laser ablation studies using a depth profiling approach (Kearns et al., 2023), but has, until now, not been shown for such a wide selection of elements. The cause of this behaviour in Mg/Ca is debated with some studies suggesting that, because Mg/Ca is a proxy for water

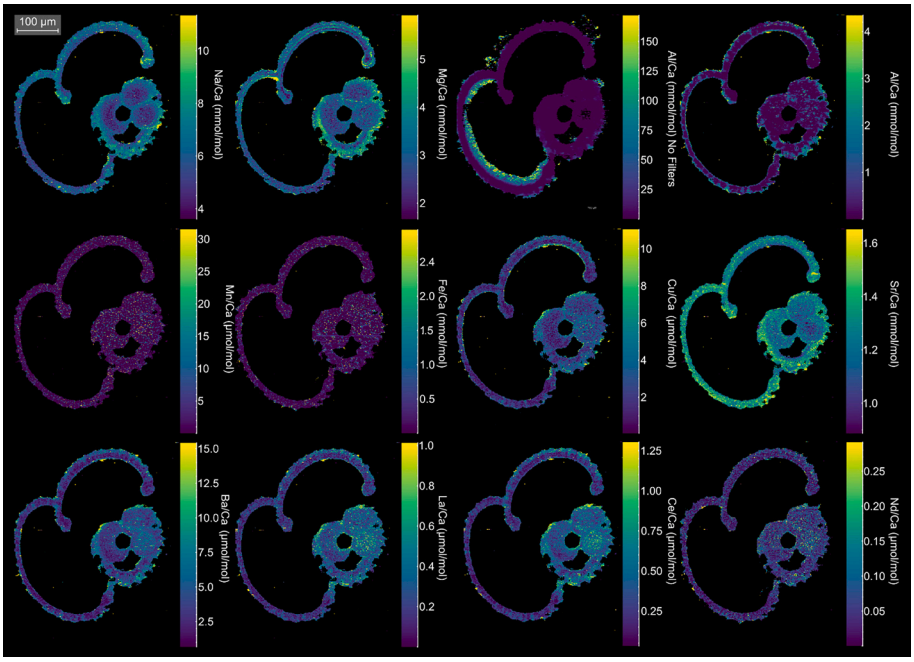

Fig. 8. Geochemical images of *Globigerinoides ruber* (sensu stricto) foraminifera test F8–2. Iolite filters applied: 'mask' on Al27 input channel applied (>80,000 cps) to screen mineralised coating on surface of test, and 'replace null'.

temperature (Anand et al., 2003), it reflects a migration of the foraminifera to deeper and colder waters towards the end of their life cycle (Pracht et al., 2019). However, final chamber depletion in Mg/Ca is also seen in lab-grown and plankton-tow samples (Bolton et al., 2011; Dueñas-Bohórquez et al., 2011), suggesting this pattern is instead related to changes in the biomineralisation process. The existence of final-chamber depletion in elements other than Mg/Ca observed here supports this latter assertion.

A commonly observed feature in a number of foraminiferal species, including *Globigerinoides ruber* (Sadekov et al., 2005), is banding in Mg/Ca and this is well developed in the *Globigerinoides ruber* analysed here, particular in the outermost chamber (Fig. 8). We also see a similar banding in Sr/Ca, and Na/Ca, that has also been observed in previous studies (Bonnin et al., 2019; Branson et al., 2016). Branson et al. (2016) also noted significant Na/Ca enrichment in the outer wall of the test of *Orbulina universa* associated with the position of spines. Like *Orbulina universa*, *Globigerinoides ruber* is a spinose species and although spines are rarely preserved in fossil specimens, it is likely the variation we see in Na/Ca perpendicular to the outer test wall also reflects the position of spines on the living specimen in this sample (Fig. 8). Our TOF-ICP-MS maps show, for the first time, that Ba/Ca, Ce/Ca, and La/Ca show similar patterns to Na/Ca.

No attempt here was made to physically remove the Fe-Mn oxyhydroxide coating that often occur on foraminifera from deep sea sediments during burial (Barker et al., 2003). These are known to be enriched in REEs (Vance et al., 2004), and although our Al/Ca mask has effectively removed the outer coatings (Fig. 8), patches of Fe and Al enrichment remain associated with elevated Cu/Ca (and other metals), LREEs such as La/Ca, Ce/Ca, and Nd/Ca along with some heavy REEs as well (e.g. Gd, Yb; see Supplementary Fig. S11). Despite this minor contamination, we show for the first time that considerable variation in the REEs within the test also occurs, with banding and variation from chamber to chamber (Fig. 8).

3.2.5. *Coralline algae Boreolithothamnion cf. soriferum*

A 0.508 by 1.064 mm area of *Boreolithothamnion* cf. *soriferum* CS9 was imaged using a 2 by 2 µm square laser beam with 1 µm spacing, tracking at a speed of 200 µm s^{-1} (Fig. 9, see also Supplementary Fig. S12). Mg/Ca in the skeletons of coralline algae is often used as a proxy for temperature, being enriched during warmer summer months (Halfar et al., 2000; Kamenos et al., 2008; Kamenos, 2010). The Mg/Ca banding observed here is consistent with previous studies (Kamenos and Law, 2010; Melbourne et al., 2023), with the narrowness of the low Mg/Ca bands indicating slower winter growth. The Sr/Ca and Mg/Ca

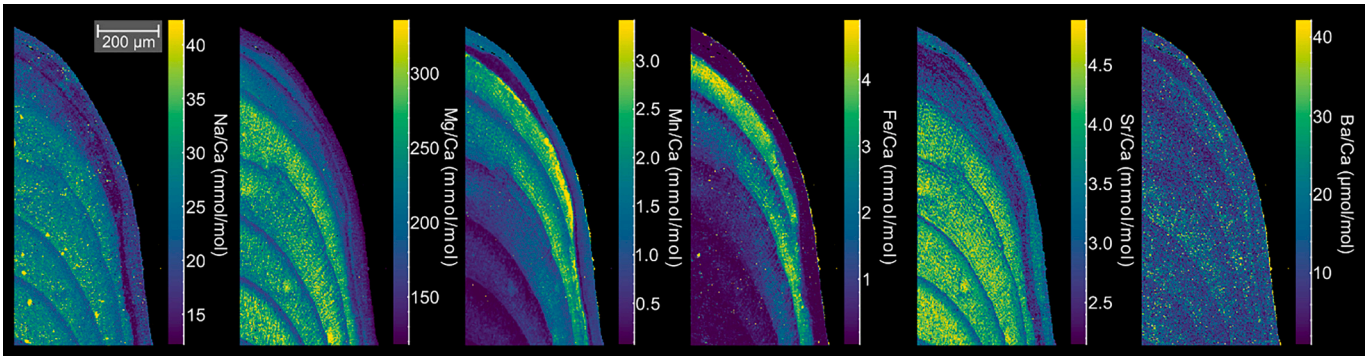

Fig. 9. Geochemical images of coralline algae *Boreolithothamnion* cf. *soriferum* skeleton CS9. No filters were applied to these images in Iolite.

variations observed closely parallel those observed in a LA-ICP-MS study of by Hetzinger et al. (2011) that showed Sr/Ca closely follows the banding pattern found with Mg/Ca, implying Sr/Ca also follows temperature trends, as suggested by Kolzenburg et al. (2023).

Our TOF-ICP-MS maps also reveal considerable annual variation in several other elements, such as Na/Ca, Mn/Ca, Ba/Ca, and Fe/Ca, which are thus far underappreciated in the literature. Although the significance of these variations is currently unclear, their patterns clearly exhibit a clear seasonal control. Chan et al. (2011) showed that in *Clathromorphum nereostratum,* higher Ba/Ca appears to correspond to greater inputs of riverine freshwater, similar to what is seen in tropical corals (see above). No river gauge data is currently available for Loch Sween, but in this location freshwater input is likely highest in the winter suggesting some other control on Ba/Ca in *Boreolithothamnion* cf. *soriferum,* although there could be a slight increase in freshwater input due to snowmelt in the spring. Previous work by Hetzinger et al. (2011) found a weak correlation between sea surface temperature and Ba/Ca, suggesting no direct relationship of algal Ba/Ca variation and seawater temperature. However, our images show that Ba/Ca in *Boreolithothamnion* cf. *soriferum* exhibits a good correlation with Mg/Ca, suggesting a potential link between Ba/Ca and environmental factors, possibly temperature. Mn/Ca and Fe/Ca are higher in recent growth, in contrast to the more consistent repeating patterns of Na/Ca, Mg/Ca, and Sr/Ca, implying a possible recent change in Fe and Mn uptake. The general elevated Fe/Ca and Mn/Ca in summer growth (Fig. 9) align with thermodynamic expectations, as incorporation of both Fe and Mn into calcite increases with increasing temperature (Dromgoole and Walter, 1990), thus like Mg/Ca and Sr/Ca, both Fe/Ca and Mn/Ca in *Boreolithothamnion* cf. *soriferum* likely have some temperature dependency.

4. Conclusions

We show here for the first time that the Nu Vitesse TOF-ICP-MS, when coupled with the ESL ImageGeo193nm laser system with Two-Vol3 ablation cell, is capable of generating accurate 2D maps of marine biogenic carbonates at an unprecedented spatial resolution ($\leq$2 μm pixel width) and rate (200 pixel/s). The upper (~0.15 to 30 wt% at high and low mass respectively) and lower (0.5 μg g^{-1}) LoQ, is sufficient to simultaneously quantify and image elements present at major (e.g. Ca, Mg, Sr, Na) and trace quantities (e.g. Ba, La, U). These features make the LA-TOF-ICP-MS approach we outline a viable alternative to the current tools available for the 2D mapping of marine biominerals but has the advantage of being sufficiently rapid to facilitate the imaging of large target areas (e.g. several mm^2 at 1 μm pixel widths) and/or large populations of individuals (e.g. 1 entire foraminifera imaged in 1 h). Because the TOF-ICP-MS collects all elements, not just a pre-defined list, the 2D maps we present here clearly demonstrate that a high-degree of heterogeneity exists in nearly all quantified elements (except Ca) at the micron-scale. Indeed, it appears that variability (CV >0.1) at micron-scale is the norm in naturally grown marine biogenic carbonates. This level of heterogeneity clearly presents a challenge for high-resolution climate reconstructions based on micro-sampling, but at the same time offers an opportunity to study and potentially quantify the physiological processes that drive these observed vital effects.

CRediT authorship contribution statement

Christopher D. Standish: Writing – review & editing, Writing – original draft, Visualization, Validation, Software, Methodology, Investigation, Formal analysis, Data curation, Conceptualization. **J. Andy Milton:** Writing – review & editing, Resources, Methodology, Investigation, Formal analysis, Conceptualization. **Tessa M. Page:** Writing – review & editing, Writing – original draft, Investigation. **Rachel M. Brown:** Writing – review & editing, Formal analysis. **David Douglas:** Writing – review & editing, Methodology. **Bence Paul:** Writing – review & editing, Software. **Lukas Schlatt:** Methodology, Writing – review & editing. **Gavin L. Foster:** Writing – review & editing, Writing – original draft, Project administration, Methodology, Investigation, Funding acquisition, Conceptualization.

Declaration of competing interest

D. Douglas is employed by Elemental Scientific Lasers LLC who loaned the imageGEO193 laser ablation system used in this study and aided with setting up and optimising the laser ablation system. B. Paul is employed by Elemental Scientific Lasers LLC, vendors of the Iolite software package, and aided with using this software. L. Schlatt is employed by Nu Instruments, the manufacturers of the Vitesse Time-of-Flight ICP mass spectrometer used in this study, and aided with setting up and optimising the TOF mass spectrometer as well as revising the manuscript. None of these employments change the results or any of the conclusions of this contribution, and the study would have produced the same outcomes. All other authors declare no competing interests.

Data availability

The raw data that support the findings of this study are available from the corresponding author, [CDS], upon reasonable request.

Acknowledgements

Karl Castillo, Justin Ries, Nick Kamenos, Ellen MacDonald, Laura Robinson, and Joe Stewart are all thanked for supplying samples used in this study, whilst Dan Doran is thanked for sample preparation prior to LA-TOF-ICP-MS. Phil Shaw is acknowledged for his assistance in set-up and optimisation of the Vitesse TOF-ICP-MS. This work was funded by the ERC Advanced Grant Micons2Reefs (#884650) awarded to GLF, supporting CDS and TMP, and NERC Grant (NE/T008814/1) awarded to GLF and JAM that funded the purchase of the Vitesse TOF-ICP-MS.

Appendix A. Supplementary data

Supplementary data to this article can be found online at https://doi.org/10.1016/j.chemgeo.2024.122438.

References

Addadi, L., Raz, S., Weiner, S., 2003. Taking advantage of disorder: amorphous calcium carbonate and its roles in biomineralization. Adv. Mater. 15, 959–970. https://doi.org/10.1002/adma.200300381.

Aizawa, S., 2008. Determination of trace elements in carbonate reference samples by instrumental neutron activation analysis. J. Radioanal. Nucl. Chem. 278, 349–352. https://doi.org/10.1007/s10967-008-9608-y.

Almirall, J.R., Trejos, T., 2016. Applications of LA–ICP–MS to forensic science. Elements 12, 335–340. https://doi.org/10.2113/gselements.12.5.335.

Anand, P., Elderfield, H., Conte, M.H., 2003. Calibration of Mg/Ca thermometry in planktonic foraminifera from a sediment trap time series. Paleoceanography 18. https://doi.org/10.1029/2002PA000846.

Aonishi, T., Hirata, T., Kuwatani, T., Fujimoto, M., Chang, Q., Kimura, J.-I., 2018. A numerical inversion method for improving the spatial resolution of elemental imaging by laser ablation-inductively coupled plasma-mass spectrometry. J. Anal. Spectrom. 33, 2210–2218. https://doi.org/10.1039/C7JA00334J.

Balestra, B., Rose, T., Fehrenbacher, J., Knobelspiesse, K.D., Huber, B.T., Gooding, T., Paytan, A., 2021. In situ Mg/Ca measurements on foraminifera: comparison between laser ablation inductively coupled plasma mass spectrometry and wavelength-dispersive x-ray spectroscopy by electron probe microanalyzer. Geochem. Geophys. Geosyst. 22, e2020GC009449. https://doi.org/10.1029/2020GC009449.

Barbosa, L.D., Sussulini, A., 2019. Recent advances in LA-ICP-MS for biomedical applications. Biomed. Spectrosc. Imaging 8, 47–54. https://doi.org/10.3233/BSI-200193.

Barker, S., Greaves, M., Elderfield, H., 2003. A study of cleaning procedures used for foraminiferal Mg/Ca paleothermometry. Geochem. Geophys. Geosyst. 4. https://doi.org/10.1029/2003GC000559.

Boer, W., Nordstad, S., Weber, M., Mertz-Kraus, R., Hönisch, B., Bijma, J., Raitzsch, M., Wilhelms-Dick, D., Foster, G.L., Goring-Harford, H., Nürnberg, D., Hauff, F., Kuhnert, H., Lugli, F., Spero, H., Rosner, M., van Gaever, P., de Nooijer, L.J., Reichart, G.-J., 2022. New calcium carbonate nano-particulate pressed powder pellet (NFHS-2-NP) for LA-ICP-OES, LA-(MC)-ICP-MS and μXRF. Geostand. Geoanal. Res. 46, 411–432. https://doi.org/10.1111/ggr.12425.

Bolton, A., Baker, J.A., Dunbar, G.B., Carter, L., Smith, E.G.C., Neil, H.L., 2011. Environmental versus biological controls on Mg/Ca variability in Globigerinoides ruber (white) from core top and plankton tow samples in the Southwest Pacific Ocean. Paleoceanography 26. https://doi.org/10.1029/2010PA001924.

Bonnin, E.A., Zhu, Z., Fehrenbacher, J.S., Russell, A.D., Hönisch, B., Spero, H.J., Gagnon, A.C., 2019. Submicron sodium banding in cultured planktic foraminifera shells. Geochim. Cosmochim. Acta 253, 127–141. https://doi.org/10.1016/j.gca.2019.03.024.

Branson, O., 2018. Boron incorporation into marine CaCO3. Adv. Isot. Geochem. 71–105. https://doi.org/10.1007/978-3-319-64666-4_4.

Branson, O., Redfern, S.A.T., Tyliszczak, T., Sadekov, A., Langer, G., Kimoto, K., Elderfield, H., 2013. The coordination of Mg in foraminiferal calcite. Earth Planet. Sci. Lett. 383, 134–141. https://doi.org/10.1016/j.epsl.2013.09.037.

Branson, O., Bonnin, E.A., Perea, D.E., Spero, H.J., Zhu, Z., Winters, M., Hönisch, B., Russell, A.D., Fehrenbacher, J.S., Gagnon, A.C., 2016. Nanometer-scale chemistry of a calcite biomineralization template: implications for skeletal composition and nucleation. Proc. Natl. Acad. Sci. 113, 12934–12939. https://doi.org/10.1073/pnas.1522864113.

Chalk, T.B., Standish, C.D., D'Angelo, C., Castillo, K.D., Milton, J.A., Foster, G.L., 2021. Mapping coral calcification strategies from in situ boron isotope and trace element measurements of the tropical coral Siderastrea siderea. Sci. Rep. 11. https://doi.org/10.1038/s41598-020-78778-1.

Chan, P., Halfar, J., Williams, B., Hetzinger, S., Steneck, R., Zack, T., Jacob, D.E., 2011. Freshening of the Alaska Coastal current recorded by coralline algal Ba/Ca ratios. J. Geophys. Res. Biogeosci. 116. https://doi.org/10.1029/2010JG001548.

Chen, S., Littley, E.F.M., Rae, J.W.B., Charles, C.D., Adkins, J.F., 2021. Uranium distribution and incorporation mechanism in deep-sea corals: implications for seawater [CO32 –] proxies. Front. Earth Sci. 9, 641327. https://doi.org/10.3389/feart.2021.641327.

Chen, S., Littley, E.F.M., Rae, J.W.B., Charles, C.D., Guan, Y., Adkins, J.F., 2023. Coherent tracer correlations in deep-sea corals and implications for biomineralization mechanisms underlying vital effects. Geochim. Cosmochim. Acta 343, 304–322. https://doi.org/10.1016/j.gca.2022.12.006.

D'Agostino, R.B., 1970. Transformation to normality of the null distribution of g1. Biometrika 57, 679–681. https://doi.org/10.1093/biomet/57.3.679.

DeLong, K.L., Maupin, C.R., Flannery, J.A., Quinn, T.M., Shen, C.-C., 2016. Refining temperature reconstructions with the Atlantic coral Siderastrea siderea. Palaeogeogr. Palaeoclimatol. Palaeoecol. 462, 1–15. https://doi.org/10.1016/j.palaeo.2016.08.028.

Dromgoole, E.L., Walter, L.M., 1990. Iron and manganese incorporation into calcite: Effects of growth kinetics, temperature and solution chemistry. Chem. Geol. 81, 311–336. https://doi.org/10.1016/0009-2541(90)90053-A.

Dueñas-Bohórquez, A., Rocha, R.E., Kuroyanagi, A., Nooijer, L.J., Bijma, J., Reichart, G.-J., 2011. Interindividual variability and ontogenetic effects on Mg and Sr incorporation in the planktonic foraminifer Globigerinoides sacculifer. Geochim. Cosmochim. Acta 75, 520–532. https://doi.org/10.1016/j.gca.2010.10.006.

Eggins, S.M., Sadekov, A., Deckker, P.D., 2004. Modulation and daily banding of Mg/Ca in Orbulina universa tests by symbiont photosynthesis and respiration: a complication for seawater thermometry? Earth Planet. Sci. Lett. 225, 411–419. https://doi.org/10.1016/j.epsl.2004.06.019.

Elderfield, H., Ferretti, P., Greaves, M., Crowhurst, S., McCave, I.N., Hodell, D., Piotrowski, A.M., 2012. Evolution of ocean temperature and ice volume through the Mid-Pleistocene climate transition. Science 337, 704–709. https://doi.org/10.1126/science.1221294.

Erez, J., 2003. The source of ions for biomineralization in foraminifera and their implications for paleoceanographic proxies. Rev. Mineral. Geochem. 54, 115–149. https://doi.org/10.2113/0540115.

Fehrenbacher, J.S., Martin, P.A., 2014. Exploring the dissolution effect on the intrashell Mg/Ca variability of the planktic foraminifer Globigerinoides ruber. Paleoceanography 29, 854–868. https://doi.org/10.1002/2013PA002571.

Fehrenbacher, J., Marchitto, T., Spero, H.J., 2020. Comparison of laser ablation and solution-based ICP-MS results for individual foraminifer Mg/Ca and Sr/Ca analyses. Geochem. Geophys. Geosyst. 21, e2020GC009254. https://doi.org/10.1029/2020GC009254.

Fietzke, J., Wall, M., 2022. Distinct fine-scale variations in calcification control revealed by high-resolution 2D boron laser images in the cold-water coral *Lophelia pertusa*. Sci. Adv. 8, eabj4172. https://doi.org/10.1126/sciadv.abj4172.

Fietzke, J., Ragazzola, F., Halfar, J., Dietze, H., Foster, L.C., Hansteen, T.H., Eisenhauer, A., Steneck, R.S., 2015. Century-scale trends and seasonality in pH and temperature for shallow zones of the Bering Sea. Proc. Natl. Acad. Sci. 112, 2960–2965. https://doi.org/10.1073/pnas.1419216112.

Flierdt, T., Robinson, L.F., Adkins, J.F., 2010. Deep-sea coral aragonite as a recorder for the neodymium isotopic composition of seawater. Geochim. Cosmochim. Acta 74, 6014–6032. https://doi.org/10.1016/j.gca.2010.08.001.

Flöter, S., Fietzke, J., Gutjahr, M., Nehrke, G., Eisenhauer, A., 2022. Incorporation of Na and S in bamboo coral skeletons. Chem. Geol. 597, 120795. https://doi.org/10.1016/j.chemgeo.2022.120795.

Fowell, S.E., Sandford, K., Stewart, J.A., Castillo, K.D., Ries, J.B., Foster, G.L., 2016. Intrareef variations in Li/Mg and Sr/Ca sea surface temperature proxies in the Caribbean reef-building coral Siderastrea siderea. Paleoceanography 31, 1315–1329. https://doi.org/10.1002/2016PA002968.

Gagnon, A.C., Adkins, J.F., Fernandez, D.P., Robinson, L.F., 2007. Sr/Ca and Mg/Ca vital effects correlated with skeletal architecture in a scleractinian deep-sea coral and the role of Rayleigh fractionation. Earth Planet. Sci. Lett. 261, 280–295. https://doi.org/10.1016/j.epsl.2007.07.013.

Gilbert, P.U.P.A., Bergmann, K.D., Boekelheide, N., Tambutté, S., Mass, T., Marin, F., Adkins, J.F., Erez, J., Gilbert, B., Knutson, V., Cantine, M., Hernández, J.O., Knoll, A. H., 2022. Biomineralization: Integrating mechanism and evolutionary history. Sci. Adv. 8. https://doi.org/10.1126/sciadv.abl9653.

Gundlach-Graham, A., Günther, D., 2016. Toward faster and higher resolution LA–ICPMS imaging: on the co-evolution of LA cell design and ICPMS instrumentation. Anal. Bioanal. Chem. 408, 2687–2695. https://doi.org/10.1007/s00216-015-9251-8.

Halfar, J., Zack, T., Kronz, A., Zachos, J.C., 2000. Growth and high-resolution paleoenvironmental signals of rhodoliths (coralline red algae): a new biogenic archive. J. Geophys. Res. Oceans 105, 22107–22116. https://doi.org/10.1029/1999JC000128.

Henehan, M.J., Foster, G.L., Rae, J.W.B., Prentice, K.C., Erez, J., Bostock, H.C., Marshall, B.J., Wilson, P.A., 2015. Evaluating the utility of B/Ca ratios in planktic foraminifera as a proxy for the carbonate system: a case study of Globigerinoides ruber. Geochem. Geophys. Geosyst. 16, 1052–1069. https://doi.org/10.1002/2014GC005514.

Hetzinger, S., Halfar, J., Zack, T., Gamboa, G., Jacob, D.E., Kunz, B.E., Kronz, A., Adey, W., Lebednik, P.A., Steneck, R.S., 2011. High-resolution analysis of trace elements in crustose coralline algae from the North Atlantic and North Pacific by laser ablation ICP-MS. Palaeogeogr. Palaeoclimatol. Palaeoecol. 302, 81–94. https://doi.org/10.1016/j.palaeo.2010.06.004.

Inoue, M., Nohara, M., Okai, T., Suzuki, A., Kawahata, H., 2004. Concentrations of trace elements in carbonate reference materials coral JCp-1 and giant clam JCt-1 by inductively coupled plasma-mass spectrometry. Geostand. Geoanal. Res. 28, 411–416. https://doi.org/10.1111/j.1751-908X.2004.tb00759.x.

Jochum, K.P., Garbe-Schönberg, D., Veter, M., Stoll, B., Weis, U., Weber, M., Lugli, F., Jentzen, A., Schiebel, R., Wassenburg, J.A., Jacob, D.E., Haug, G.H., 2019. Nano-powdered calcium carbonate reference materials: significant progress for microanalysis? Geostand. Geoanal. Res. 43, 595–609. https://doi.org/10.1111/ggr.12292.

John, E.H., Staudigel, P.T., Buse, B., Lear, C.H., Pearson, P.N., Slater, S.M., 2023. Revealing their true stripes: Mg/Ca banding in the paleogene planktonic foraminifera genus morozovella and implications for paleothermometry. Paleoceanogr. Paleoclimatol. 38, e2023PA004652. https://doi.org/10.1029/2023PA004652.

Kamenos, N.A., 2010. North Atlantic summers have warmed more than winters since 1353, and the response of marine zooplankton. Proc. Natl. Acad. Sci. 107, 22442–22447. https://doi.org/10.1073/pnas.1006141107.

Kamenos, N.A., Law, A., 2010. Temperature controls on coralline algal skeletal growth. J. Phycol. 46, 331–335. https://doi.org/10.1111/j.1529-8817.2009.00780.x.

Kamenos, N.A., Cusack, M., Moore, P.G., 2008. Coralline algae are global palaeothermometers with bi-weekly resolution. Geochim. Cosmochim. Acta 72, 771–779. https://doi.org/10.1016/j.gca.2007.11.019.

Kearns, L.E., Searle-Barnes, A., Foster, G.L., Milton, J.A., Standish, C.D., Ezard, T.H.G., 2023. The influence of geochemical variation among globigerinoides ruber individuals on paleoceanographic reconstructions. Paleoceanogr. Paleoclimatol. 38, e2022PA004549. https://doi.org/10.1029/2022PA004549.

Kershaw, J., Stewart, J.A., Strawson, I., Ferreira, M.L.C., Robinson, L.F., Hendry, K.R., Samperiz, A., Burke, A., Rae, J.W.B., Day, R.D., Etnoyer, P.J., Williams, B., Häussermann, V., 2023. Ba/Ca of stylasterid coral skeletons records dissolved seawater barium concentrations. Chem. Geol. 622, 121355. https://doi.org/10.1016/j.chemgeo.2023.121355.

Kolzenburg, R., Moreira, H., Storey, C., Ragazzola, F., 2023. Structural integrity and skeletal trace elements in intertidal coralline algae across the Northeast Atlantic reveal a distinct separation of the leading and the trailing edge populations. Mar. Environ. Res. 190, 106086. https://doi.org/10.1016/j.marenvres.2023.106086.

Komsta, L., Novomestky, F., 2015. Moments, cumulants, skewness, kurtosis and related tests. R Pack. Vers. 14.

Limburg, K.E., Huang, R., Bilderback, D.H., 2007. Fish otolith trace element maps: new approaches with synchrotron microbeam x-ray fluorescence. X-Ray Spectrom. 36, 336–342. https://doi.org/10.1002/xrs.980.

Limburg, K.E., Olson, C., Walther, Y., Dale, D., Slomp, C.P., Høie, H., 2011. Tracking baltic hypoxia and cod migration over millennia with natural tags. Proc. Natl. Acad. Sci. 108, E177–E182. https://doi.org/10.1073/pnas.1100684108.

Lockwood, T.E., Gonzalez de Vega, R., Du, Z., Schlatt, L., Xu, X., Clases, D., 2024. Strategies to enhance figures of merit in ICP-ToF-MS. J. Anal. Spectrom. 39, 227–234. https://doi.org/10.1039/D3JA00288H.

MacDonald, E., Foster, G.L., Standish, C.D., Trend, J., Kamenos, N., 2024. Historic Ocean Acidification of Loch Sween revealed by correlative geochemical imaging and high-resolution boron isotope analysis of *Boreolithothamnion* cf. *soriferum*. Earth Planet. Sci. Lett. 646, 118976. https://doi.org/10.1016/j.epsl.2024.118976.

McCulloch, M., Fallon, S., Wyndham, T., Hendy, E., Lough, J., Barnes, D., 2003. Coral record of increased sediment flux to the inner Great Barrier Reef since European settlement. Nature 421, 727–730. https://doi.org/10.1038/nature01361.

Meibom, A., Cuif, J.-P., Hillion, F., Constantz, B.R., Juillet-Leclerc, A., Dauphin, Y., Watanabe, T., Dunbar, R.B., 2004. Distribution of magnesium in coral skeleton. Geophys. Res. Lett. 31, 1–4. https://doi.org/10.1029/2004GL021313.

Meibom, A., Cuif, J.-P., Houlbreque, F., Mostefaoui, S., Dauphin, Y., Meibom, K.L., Dunbar, R., 2008. Compositional variations at ultra-structure length scales in coral skeleton. Geochim. Cosmochim. Acta 72, 1555–1569. https://doi.org/10.1016/j.gca.2008.01.009.

Melbourne, L.A., Brodie, J., Rayfield, E.J., Titelboim, D., Lord, O.T., Schmidt, D.N., 2023. Environmental impacts on the structural integrity of British rhodoliths. Sci. Rep. 13, 13473. https://doi.org/10.1038/s41598-023-40292-5.

Müller, W., Fietzke, J., 2016. The role of LA–ICP–MS in palaeoclimate research. Elements 12, 329–334. https://doi.org/10.2113/gselements.12.5.329.

Nambiar, R., Müller, W., Eavans, D., 2024. Evaluating accuracy improvements of laser ablation ICPMS element analysis in silicate glasses and carbonates via downhole fractionation correction – an old problem re-assessed. J. Anal. At. Spectrom. 39, 1454–1460. https://doi.org/10.1039/D4JA00018H.

Nash, M.C., Diaz-Pulido, G., Harvey, A.S., Adey, W., 2019. Coralline algal calcification: a morphological and process-based understanding. PLoS One 14, 1–61. https://doi.org/10.1371/journal.pone.0221396.

Nothdurft, L.D., Webb, G.E., 2007. Microstructure of common reef-building coral genera Acropora, Pocillopora, Goniastrea and Porites: constraints on spatial resolution in geochemical sampling. Facies 53, 1–26. https://doi.org/10.1007/s10347-006-0090-0.

Okai, T., Suzuki, A., Kawahata, H., Terashima, S., Imai, N., 2002. Preparation of a new geological survey of Japan geochemical reference material: coral JCp-1. Geostand. Newslett. 26, 95–99. https://doi.org/10.1111/j.1751-908X.2002.tb00627.x.

Paton, C., Hellstrom, J., Paul, B., Woodhead, J., Hergt, J., 2011. Iolite: Freeware for the visualisation and processing of mass spectrometric data. J. Anal. Spectrom. 26, 2508–2518. https://doi.org/10.1039/C1JA10172B.

Politi, Y., Batchelor, D.R., Zaslansky, P., Chmelka, B.F., Weaver, J.C., Sagi, I., Weiner, S., Addadi, L., 2010. Role of magnesium ion in the stabilization of biogenic amorphous calcium carbonate: a structure−function investigation. Chem. Mater. 22, 161–166. https://doi.org/10.1021/cm902674h.

Pracht, H., Metcalfe, B., Peeters, F.J.C., 2019. Oxygen isotope composition of the final chamber of planktic foraminifera provides evidence of vertical migration and depth-integrated growth. Biogeosciences 16, 643–661. https://doi.org/10.5194/bg-16-643-2019.

Robinson, L.F., Adkins, J.F., Fernandez, D.P., Burnett, D.S., Wang, S.-L., Gagnon, A.C., Krakauer, N., 2006. Primary U distribution in scleractinian corals and its implications for U series dating. Geochem. Geophys. Geosyst. 7, Q05022. https://doi.org/10.1029/2005GC001138.

Sadekov, A.Yu., Eggins, S.M., De Deckker, P., 2005. Characterization of Mg/Ca distributions in planktonic foraminifera species by electron microprobe mapping. Geochem. Geophys. Geosyst. 6. https://doi.org/10.1029/2005GC000973.

Sadekov, A., Eggins, S.M., De Deckker, P., Ninnemann, U., Kuhnt, W., Bassinot, F., 2009. Surface and subsurface seawater temperature reconstruction using Mg/Ca microanalysis of planktonic foraminifera Globigerinoides ruber, Globigerinoides sacculifer, and Pulleniatina obliquiloculata. Paleoceanography 24. https://doi.org/10.1029/2008PA001664.

Schmidt, M.W., Spero, H.J., Lea, D.W., 2004. Links between salinity variation in the Caribbean and North Atlantic thermohaline circulation. Nature 428, 160–163. https://doi.org/10.1038/nature02346.

Serrato Marks, G., LaVigne, M., Hill, T.M., Sauthoff, W., Guilderson, T.P., Roark, E.B., Dunbar, R.B., Horner, T.J., 2017. Reproducibility of Ba/Ca variations recorded by northeast Pacific bamboo corals. Paleoceanography 32, 966–979. https://doi.org/10.1002/2017PA003178.

Shaw, K.M.M., Standish, C.D., Fowell, S.E., Stewart, J.A., Castillo, K.D., Ries, J.B., Foster, G.L., 2024. Century-long records of sedimentary input on a Caribbean reef from coral Ba/Ca ratios. Paleoceanogr. Paleoclimatol. 39, e2023PA004746. https://doi.org/10.1029/2023PA004746.

Sinclair, D.J., Kinsley, L.P.J., Mcculloch, M.T., 1998. High resolution analysis of trace elements in corals by laser ablation ICP-MS. Geochim. Cosmochim. Acta 62, 1889–1901. https://doi.org/10.1016/S0016-7037(98)00112-4.

Sinclair, D.J., Williams, B., Risk, M., 2006. A biological origin for climate signals in corals—Trace element "vital effects" are ubiquitous in Scleractinian coral skeletons. Geophys. Res. Lett. 33. https://doi.org/10.1029/2006GL027183.

Smith, A.M., Sutherland, J.E., Kregting, L., Farr, T.J., Winter, D.J., 2012. Phylomineralogy of the Coralline red algae: Correlation of skeletal mineralogy with molecular phylogeny. Phytochemistry 81, 97–108. https://doi.org/10.1016/j.phytochem.2012.06.003.

Spero, H.J., Eggins, S.M., Russell, A.D., Vetter, L., Kilburn, M.R., Hönisch, B., 2015. Timing and mechanism for intratest Mg/Ca variability in a living planktic foraminifer. Earth Planet. Sci. Lett. 409, 32–42. https://doi.org/10.1016/j.epsl.2014.10.030.

Standish, C., Dhuime, B., Chapman, R., Coath, C., Hawkesworth, C., Pike, A., 2013. Solution and laser ablation MC-ICP-MS lead isotope analysis of gold. J. Anal. Spectrom. 28, 217–225. https://doi.org/10.1039/C2JA30277B.

Standish, C.D., Trend, J., Kleboe, J., Chalk, T.B., Mahajan, S., Milton, J.A., Page, T.M., Robinson, L.F., Stewart, J.A., Foster, G.L., 2024. Correlative geochemical imaging of *Desmophyllum dianthus* reveals biomineralisation strategy as a key coral vital effect. Sci. Rep. 14, 11121. https://doi.org/10.1038/s41598-024-61772-2.

Stewart, J.A., Anagnostou, E., Foster, G.L., 2016. An improved boron isotope pH proxy calibration for the deep-sea coral Desmophyllum dianthus through sub-sampling of fibrous aragonite. Chem. Geol. 447, 148–160. https://doi.org/10.1016/j.chemgeo.2016.10.029.

Sun, C.-Y., Stifler, C.A., Chopdekar, R.V., Schmidt, C.A., Parida, G., Schoeppler, V., Fordyce, B.I., Brau, J.H., Mass, T., Tambutté, S., Gilbert, P.U.P.A., 2020. From particle attachment to space-filling coral skeletons. Proc. Natl. Acad. Sci. USA 117, 30159–30170. https://doi.org/10.1073/pnas.2012025117.

Sylvester, P.J., Jackson, S.E., 2016. A brief history of laser ablation inductively coupled plasma mass spectrometry (LA–ICP–MS). Elements 12, 307–310. https://doi.org/10.2113/gselements.12.5.307.

Thompson, D.M., 2022. Environmental records from coral skeletons: a decade of novel insights and innovation. Wiley Interdiscip. Rev. Clim. Chang. 13. https://doi.org/10.1002/wcc.745.

Urey, H.C., Lowenstam, H.A., Epstein, S., McKinney, C.R., 1951. Measurement of paleotemperatures and temperatures of the Upper Cretaceous of England, Denmark, and the southeastern United States. GSA Bull. 62, 399–416. https://doi.org/10.1130/0016-7606(1951)62[399:MOPATO]2.0.CO;2.

van Elteren, J.T., Šala, M., Šelih, V.S., 2018. Perceptual image quality metrics concept in continuous scanning 2D laser ablation-inductively coupled plasma mass spectrometry bioimaging. Anal. Chem. 90, 5916–5922. https://doi.org/10.1021/acs.analchem.8b00751.

Van Malderen, S.J.M., Managh, A.J., Sharp, B.L., Vanhaecke, F., 2016. Recent developments in the design of rapid response cells for laser ablation-inductively coupled plasma-mass spectrometry and their impact on bioimaging applications. J. Anal. At. Spectrom. 31, 423–439. https://doi.org/10.1039/C5JA00430F.

Van Malderen, S.J.M., Van Acker, T., Vanhaecke, F., 2020. Sub-micrometer nanosecond LA-ICP-MS imaging at pixel acquisition rates above 250 Hz via a low-dispersion setup. Anal. Chem. 92, 5756–5764. https://doi.org/10.1021/acs.analchem.9b05056.

Vance, D., Scrivner, A.E., Beney, P., Staubwasser, M., Henderson, G.M., Slowey, N.C., 2004. The use of foraminifera as a record of the past neodymium isotope composition of seawater. Paleoceanography 19. https://doi.org/10.1029/2003PA000957.